Importance of Gas-Phase Kinetics within the Anode Channel of a Solid-Oxide Fuel Cell

Chad Y. Sheng[†] and Anthony M. Dean*

Department of Chemical Engineering, Colorado School of Mines, Golden, Colorado 80401

Received: December 12, 2003; In Final Form: February 27, 2004

Experiments using *n*-butane as a representative hydrocarbon fuel were conducted under gas-phase conditions similar to those expected in the anode channel of a solid-oxide fuel cell (SOFC). Butane conversion and product formation were monitored in quartz reactor experiments at $P \sim 0.8$ atm, $\tau \sim 5$ s, and $T = 550-800$ °C. Three different fuel mixtures were used: neat *n*-butane, 50% *n*-C_4H_{10}/50% H_2O, and 50% *n*-C_4H_{10}/50% N_2. These experiments demonstrate that substantial gas-phase chemistry does occur and that this must be accounted for when predicting fuel cell efficiency. These data were compared to predictions using a plug-flow model that incorporated the experimentally measured temperature profile along the reactor. The reaction mechanism used for these simulations consisted of ~300 species and 2500 elementary reactions and included both pyrolysis and oxidation reactions. Comparisons of the model predictions to the experimental data show that the model, without any modifications, captures the observed strong temperature dependence of *n*-butane conversion and is also able to capture the changes in product selectivity with temperature for the neat butane and the diluted butane mixtures. The model also properly predicts the observed onset of deposit formation near 700 °C. Both conversion and selectivity are shown to be sensitive to only a very small subset of the reactions in the mechanism. Comparison of the rate coefficients of this subset to literature values, where available, are generally reasonable and suggest that this kinetic model is adequate for describing the gas-phase reactions of small hydrocarbons in the anode channels of a SOFC. Additional efforts are required to account for catalytic reactions on the surface of the porous anode.

Introduction

Fuel cell technology presents the possibility of increased energy efficiency with decreased detrimental environmental impact over conventional combustion. Solid-oxide fuel cells (SOFC), in particular, offers a very promising method for direct production of electrical energy from currently available fossil fuels, thus postponing the need to build a hydrogen delivery infrastructure. An added advantage of SOFC operation is the ability to tolerate substantial quantities of CO in the feed stream, unlike polymer electrolyte membrane (PEM) fuel cells. Hybrid SOFCs, coupled with a heat recovery system such as a gas turbine generator, have the potential for fuel-to-electricity efficiencies approaching 75−80%.[1]

A typical SOFC design consists of two channels separated by a "trilayer". This trilayer consists of the anode, electrolyte and a cathode. The anode and cathode are fabricated of ceramic−metal (cermet) materials and the electrolyte consists of a dense ceramic. The (hydrocarbon) fuel flows through the anode channel, while the (air) oxidant flows through the cathode channel. Oxygen anions are formed in the porous cathode and diffuse through the (ion selective) electrolyte. Electrochemical reactions occur in the three-phase region (electrolyte, anode, fuel) to form CO_2 and H_2O, plus electrons. The electrons flow through the anode and are collected by bipolar plates. The bipolar plates provide an efficient method to conduct current, separate the channels for the fuel and air, add physical strength and allow the SOFC to be stackable and therefore scaleable. Typical operating temperatures for SOFCs range from 700 to 1000 °C.

A complete SOFC model is very complex, requiring descriptions of kinetics in multiple phases and coupling these kinetics to multiple transport processes.[2] Chemical reactions within the SOFC occur in three regions: in the anode channel (gas-phase kinetics), on the surface of the porous anode (heterogeneous catalysis), and at the three-phase boundary between the anode and electrolyte (electrochemical catalysis). Thus, the homogeneous and heterogeneous kinetics have the potential to substantially change the nature of the species that ultimately undergo electrochemical oxidation. It is essential to account for such kinetic modifications to properly characterize SOFC operation and estimate the expected efficiency.

Another issue in SOFC operation is deposit formation. The high operating temperatures of a SOFC can lead to fuel degradation and formation of carbonaceous deposits within the fuel channels and porous anode structures. SOFCs that run on H_2 as a fuel source often utilize nickel as the electrical conductor. However, nickel is known to react with hydrocarbons to form deposits.[3] Several studies have reported on the use of different materials to minimize deposit formation[4−10] as well as upstream conversion of hydrocarbon fuels to syngas (CO and H_2) as a way to avoid deposit formation.[11−16]

An important feature of SOFC operation is the electrochemical formation of H_2O and CO_2. These species form at the three-phase boundary and will diffuse through the porous anode to the anode channel, thus diluting the fuel stream. While still in the anode, these species can participate in "internal reforming" reactions, performing the same function of converting hydrocarbon fuel to CO and H_2 that might be accomplished by the

* To whom correspondence should be addressed. E-mail: amdean@mines.edu.

[†] Current address: National Institute of Standards and Technology, Gaithersburg, MD 20899.

10.1021/jp037839w CCC: $27.50
Published on Web 04/03/2004

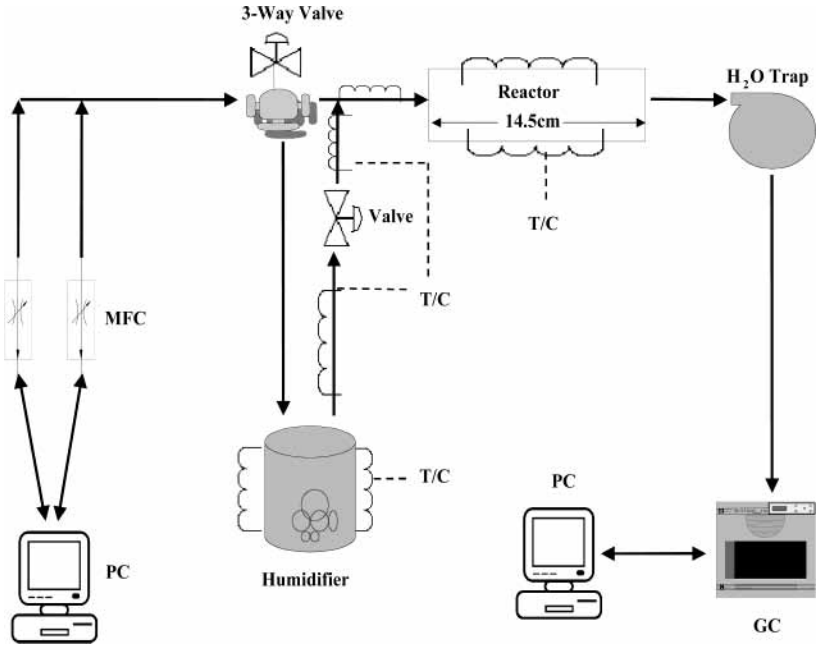

Figure 1. Experimental setup for study of *n*-butane pyrolysis under conditions similar to the anode channel of a SOFC.

upstream reforming discussed earlier. Under these conditions it is likely that the water-gas shift reaction would also take place, converting $CO + H_2O$ to $H_2 + CO_2$. These reactions can further complicate the identity of the "fuel" that will participate in the electrochemical reactions. In addition, steam gasification, to remove any deposits already formed, might be catalyzed by the metal in the anode cermet.

As a first step toward characterizing the complex kinetics, we want to make sure that we properly understand the gas-phase hydrocarbon chemistry. The effect of gas phase reactions of methane has previously been reported.[17] It was shown that the electrochemical production of H_2O and CO_2 did indeed significantly impact the predictions regarding deposit formation. In this work, we extend this approach to butane, which is significantly more reactive than methane and thus more representative of a range of hydrocarbon fuels. Furthermore, given the sparsity of available data on butane reactivity under SOFC conditions, we thought it essential to generate the requisite data to validate our kinetic model. Although numerous studies on *n*-butane oxidation in combustion environments and *n*-butane catalytic studies are available, our literature search revealed very limited experimental studies on neat *n*-butane pyrolysis. Hepp and Frey had performed experimental studies of *n*-butane at 550 °C and 160 atm in a flow reactor.[18] Weisel et al. performed experimental studies at low pressures, 10 Torr, over the temperature range 600−1300 K, with approximately 2 ms residence time.[19] Weisel et al. utilized a 10 cm length, 1.5 mm i.d. alumina tubular reactor coupled to a molecular-beam-sampling mass spectrometer. Modeling studies for neat *n*-butane were also limited; the only study we found was by Mallinson et al.[20] Mallinson et al.'s modeling conditions were over a temperature range of 200−600 °C with pressure ranging from 1 to 1000 atm in a batch reactor with a residence time in the hundreds of seconds.

Experiment Description

The experiments used *n*-butane as the fuel over a temperature range of 550−800 °C, with a nominal 5 s residence time through a tubular flow reactor operating at an ambient (high-altitude) pressure of ∼0.8 atm. The reactor used in these experiments was a 24 cm length × 6 mm i.d. (12 mm o.d.) quartz tube, which was housed within a 14.5 cm length single-zone clamshell 2.5 cm i.d. electric tube furnace equipped with a dedicated Eurotherm model 2116 digital temperature controller. The electric tube furnace had a heating zone of 11.5 cm. The product stream flowed through a water trap, which contained Drierite supplied by W. A. Hammond Drierite Co. Ltd. The dehumidified product stream then flowed to a Hewlett-Packard 5890 Series II+ gas chromatograph (GC) and then vented to a fume hood. The system was kept near atmospheric pressure (∼0.8 atm). (Refer to Figure 1 for experimental setup).

Temperature profiles for the reactor were measured with an OMEGA type K thermocouple probe that was moved axially along the reactor length. Thermocouple errors caused by radiation from the furnace wall were minimized by using a grounded sheath and with a representative flow of inert gas. The measured temperature profiles with a N_2 flow through the quartz reactor for each set point reactor temperature, i.e. 550, 600, 650, 700, and 800 °C, are shown in Figure 2a. The reactor is kept near isothermal over the midrange of the heating zone. The temperature gradients that occur during the 5 cm inlet and the 5 cm outlet serve to preheat the reactants and cool the products. Uncertainty in absolute temperature measurements is estimated to be ±1%, as specified by the thermocouple manufacturer.

Two other sets of temperature profiles were also measured. Given that pyrolysis reactions are endothermic, additional experiments at 700 °C were conducted to observe if there was a decrease in temperature along the centerline of the reactor resulting from reaction. The measured temperature profile along the quartz reactor flowing 100% *n*-C_4H_{10} is shown as the triangle symbols in Figure 2b. The 100% *n*-butane system had a lower temperature profile than the 100% N_2 system. The largest temperature difference between the 100% N_2 and 100% *n*-C_4H_{10} system is almost 30 °C near 13 cm. An expanded view of the temperature profile is shown in Figure 2c. The measured temperature profile for the 50% *n*-C_4H_{10}/50% N_2 mixture at 700 °C was, as expected, intermediate between those shown.

The *n*-butane gas is research grade (99.9%), supplied by Air Liquide. Scott Specialty Gases were used as the calibration

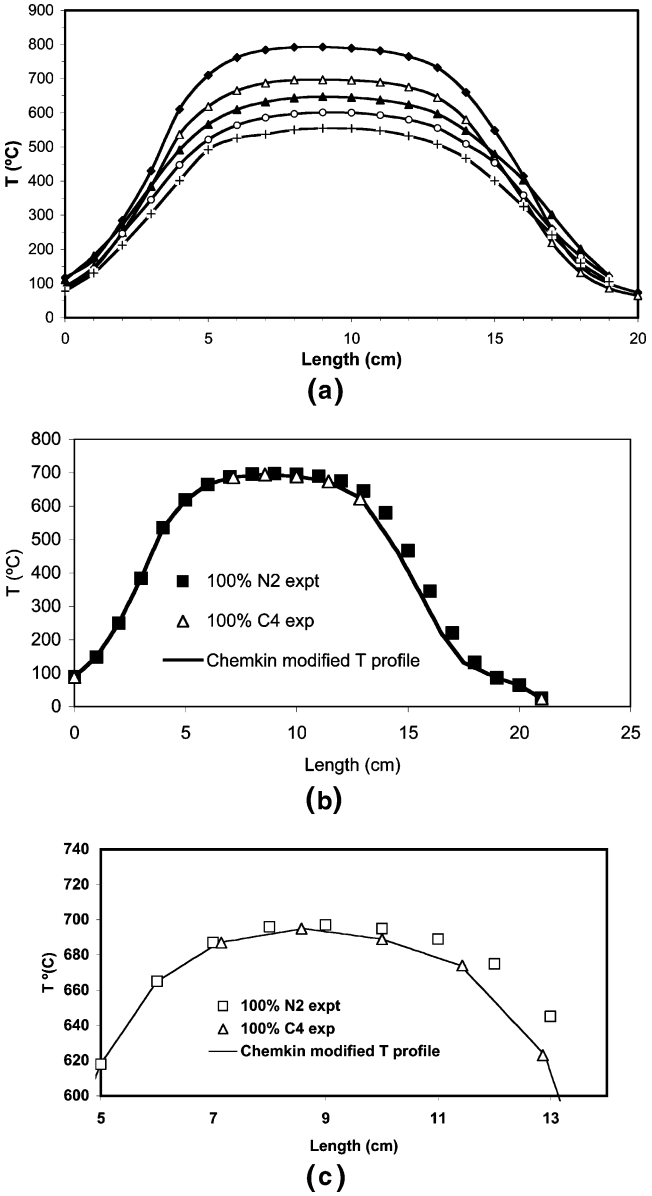

Figure 2. (a) Experimentally obtained temperature profiles along the quartz reactor with a representative N_2 flow through the system. (b) Comparison of temperature profiles at 700 °C with 100% N_2 and 100% n-C_4H_{10} flow through a quartz reactor. (c) Expanded view of part b to illustrate the deviation between the temperature profiles.

gases. General Air supplied all the other gases used. All inert gases used for the GC were 99.999% pure. MKS Instruments' mass flow controllers were used to control each of the two gas streams to the reactor. National Instrument's LabView program was used to develop a graphical user interface (GUI) and control the mass flow controllers. The inlet volumetric flow rate into the reactor for all experimental conditions was 14.6 mL min^{-1}. This flow rate provided a nominal 5 s residence time through the reactor at 550 °C and ambient pressure, with the assumption that the temperature profile is uniform and the inlet feed mixture behaves as an ideal gas.

A Hewlett-Packard 5890 Series II+ GC with two thermal conductivity detectors (TCD) was used to perform quantitative analysis of the species emerging from the reactor. Two 10-port sampling valves were used to introduce the samples into two packed columns. Each of the sampling loop volumes was 1.0 mL. A 6 ft × $^1/_8$ in. stainless steel column was packed with HayeSep R, and the second packed column was a 30 ft × $^1/_8$ in. stainless steel HayeSep DB column. The two different columns were required to identify all the measured species. Comparison of measurements made on both detectors indicated an absolute uncertainty of ~5%. Helium was used as the carrier gas for both columns as well as the reference gas for both TCDs. HP's ChemStation software package was used to acquire and quantitate the chromatograms from both detectors. Because of the carrier gas type and reference gas in the TCD, hydrogen could not be measured accurately, but the presence of hydrogen was noted in some experiments.

Three different fuel mixtures were used: neat *n*-butane (100% *n*-butane), a 50:50 *n*-butane:N_2 mixture, and a 50:50 *n*-butane:H_2O(g) mixture. For brevity, the following terminologies will be used for the remainder of this paper; the 50% *n*-butane + 50% N_2 fuel mixture will be referred to as "nC_4/N_2" and the 50% *n*-butane + 50% H_2O will be denoted as "nC_4/H_2O". The neat *n*-butane case is intended to simulate the situation near the entrance of the anode channel where little CO_2 and H_2O would be expected to be present. The nC_4/H_2O mixture represents a condition further down the channel where the products of the electrochemical reaction would be coming into the fuel stream. The nC_4/N_2 mixture was used to account for the effect of simple dilution with an inert in contrast to dilution with steam, which could possibly be a reactant.

The mass flow controllers fixed the fuel mixture composition for the nC_4/N_2 case. For the nC_4/H_2O case, a different configuration was required. The *n*-butane gas was bubbled through a sparger in a heated stainless steel evaporator, acting as a humidifier. The humidified effluent vapor composition from the evaporator was determined with the assumption that the vapor−liquid equilibrium (VLE) relationship between *n*-butane to water is similar to the VLE of air to water. The temperature at which the saturated equilibrium steam composition will be 50% at 0.8 atm is 77 °C. The flow rate of the *n*-butane through the sparger was 7.3 mL min^{-1}, with the displaced steam comprising the other 7.3 mL min^{-1} for a total volumetric flow rate of 14.6 mL min^{-1}. A dedicated Eurotherm 2116e PID temperature controller was used to regulate the vapor temperature within the humidifier chamber. Transfer lines from the humidifier are heated above 100 °C to ensure the steam did not condense prior to entering the reactor. A water trap at the exit of the reactor and prior to entrance into the GC was used, since the GC temperature program starts below 100 °C and removal of liquid water was necessary to preserve the integrity of the packed columns. Experimental runs were carried out for the three different mixtures and the five different temperature profiles. For the remainder of this paper, the temperature profiles will be referred to by their "nominal" temperatures, e.g. 600 °C means that the setting on the furnace controller was 600 °C.

Measurement of Conversion and Major Products

The experimental setup was designed to monitor the major volatile products of *n*-butane pyrolysis as well as the loss of butane. Helium was used as both the carrier gas and reference gas for the TCD to optimize detector sensitivity. However, this choice makes the detection of hydrogen in the product stream very difficult, since the thermal conductivity of hydrogen and helium are both large relative to the thermal conductivity of other gases.[21] Although the hydrogen sensitivity could have been improved by using argon, this would have decreased sensitivity for the other species, and we did not pursue this approach.

Comparison of the data for mixtures without steam to that of the steam case requires accounting for the difference in the fuel-steam experimental procedure. As pointed out earlier, this

product stream was passed through a water trap to remove the water to protect the GC columns. Thus, it is misleading to directly compare the measured GC mole fractions of the steam mixture to those of the mixtures without steam. However, it is straightforward to make the corresponding comparisons to model calculations by first subtracting the predicted steam mole fraction and then renormalizing the mole fractions of the remaining species. These can then be compared directly to the GC mole fractions measured for the steam case.

Before data were collected for a given condition, GC measurements verified that the reactor had reached steady-state operation. The effluent stream mole fractions were then measured in several repeat runs. The typical relative error in the replicate GC measurements was observed to be less that 5%. Prior to the start of an experiment, the GC sensitivity was checked by measurements on room-temperature butane; the deviations from the mean were less than 5%.

The presence of unidentified peaks in the chromatograms was observed under some high-temperature experimental conditions. The unidentified peaks that were observed had retention times that are indicative of either an unsaturated C_3 or C_4 species. However, the peak areas of these were negligible compared to the observed C_3H_6 and C_4H_{10}. Assuming that the response factors for the unidentified peaks were comparable to those measured for C_3H_6, C_3H_8, and C_4H_{10}, the unidentified peaks accounted for less than 1% of the total mole fraction. Similarly, there was no significant measurable mole fraction of any molecular weight growth species. The sum of the mole fractions for the major products observed, i.e. $x_{CH_4} + x_{C_2H_4} + x_{C_2H_6} + x_{C_3H_6}$, and that of the unreacted butane was generally measured to be close to 100%, within experimental error. This suggests that the unmeasured H_2 mole fraction is less than 5%.

Reaction Mechanism and Thermodynamic Properties

The reaction mechanism that was utilized in this study consists of 291 species and 2498 elementary reactions. It is an extension of a previous C_4 mechanism.[22] The extensions include substantially more molecular weight growth chemistry, especially involving propargyl radical pathways, and explicit inclusion of certain C_6 hydrocarbon species, including *n*-hexane, cyclohexane, and 2,3-dimethyl butane. The current mechanism is similar to the one recently used by Walters et al.[17] in their analysis of methane kinetics under SOFC conditions. The major difference is that we now have updated the butane dissociation reaction

$$C_4H_{10} \leftrightarrow 2C_2H_5$$

to reflect the recent measurement of the reverse reaction by Shafir et al.[23]

Abstraction reaction rate constants in the mechanism are based on literature data when available. If not, estimates based on the methodology described in detail by Dean and Bozzelli[24] are used. In this approach a reference reaction is selected as a model for abstraction by a specific radical, and this is used as the basis for assignment of the *A* factor (and preexponential temperature dependence) for that radical. An Evans−Polanyi analysis is used to estimate the energy of activation (E_a). The current mechanism includes abstraction reactions by H, O, OH, O_2, and selected hydrocarbon radicals.

Kineticists have long known that it is necessary to consider the pressure dependence of the rate coefficients of dissociation and recombination reactions. Similar considerations apply to any reaction that proceeds via formation of a new chemical bond. In the context of free radical chemistry, this means that one must account for the pressure dependence of radical addition to unsaturated molecules (and the reverse reaction, β-scission to form an unsaturated molecule and a radical) and insertion reactions as well as radical recombinations. Another complication in analyzing reactions proceeding via energized adducts is the possibility that additional dissociation channels to new products will be available. Thus, radical addition, recombination, and insertion reactions can manifest very complex temperature and pressure behavior as the stabilization channel competes with these multiple reaction channels. Substantial errors can result when experimental measurements of these rate coefficients are extrapolated to other regions of temperature and pressure without accounting for the competition between unimolecular reactions of the energized adducts and their bimolecular collisional stabilization. For the mechanism used in this work, we estimated these pressure dependencies using the methods described by Chang et al.[25] The current mechanism consists of approximately 200 pressure-dependent reactions.

All reactions in the mechanism are treated as reversible, using the computed equilibrium constant at the specified temperature. The thermodynamic properties for the species in the mechanism are obtained from the literature and/or estimation techniques, such as group additivity[26,27] and hydrogen bond increments for radicals.[28] No adjustments were made to the rate constants to improve the fits to the experimental data. The mechanism is in a CHEMKIN format with the rate parameters A, *n* and E_a expressed in the modified Arrhenius form, viz.

$$k = AT^n \exp(-E_a/RT)$$

The mechanism and the thermodynamic database are included in the Supporting Information.

Plug-Flow Computations

The calculations were performed using the gas-phase kinetic model with the PLUG driver program in the CHEMKIN Collection v. 3.6.2 suite programs.[29] The flow conditions in our experiments are expected to be similar to those in a SOFC anode channel. The temperature profiles used for the modeling are included in the Supporting Information. The other input parameters that are required by the PLUG subroutine were obtained directly from experimental conditions, i.e., molar composition, initial velocity/volumetric flow rate, geometric configuration of the reactor, etc.

Experimental Results

The experimental results are summarized in Table 1. Under all circumstances, there were only four major products observed: methane, ethane, ethylene, and propylene. Note that, within experimental error, the sum of the measured mole fractions of these species, plus unreacted butane is generally close to 100%, suggesting that the unmeasured hydrogen plus any other hydrocarbons constitute less than 5% of the total effluent. The higher sum observed at 700 °C suggests a small systematic error in these measurements.

550 °C. Very little conversion was observed at 550 °C, with only 1−2% conversion for both neat butane and butane/steam mixtures. In both mixtures we also see that the major products are methane and propylene, while smaller amounts of ethane and ethylene are formed, with no discernible differences between the two mixtures.

TABLE 1: Predicted and Observed Species Mole Fractions (in %) at the Effluent of the 21 cm Length Quartz Reactor for the Three Mixtures at the Nominal Temperatures[c]

inlet fuel	N_2	H_2O	CH_4	C_2H_4	C_2H_6	C_3H_6	n-C_4H_{10}	H_2	C_5^+ [a]	C_4^- [b]	Σx_i
					550 °C						
n-C_4H_{10}			0.8	0.4	0.4	0.8	97.6	0.0	4.8E−05	1.7E−02	
			0.6 ± 0.1	***0.4 ± 0.1***	***0.3 ± 0.1***	***0.8 ± 0.1***	***98.8 ± 5.0***				***100.9 ± 5.0***
n-C_4H_{10}:H_2O (0.5:0.5)		49.8	0.3	0.1	0.1	0.3	49.4	0.0	9.9E−06	5.9E−04	
			(0.5)	(0.3)	(0.3)	(0.5)	(98.4)				
			0.6 ± 0.1	***0.4 ± 0.1***	***0.3 ± 0.1***	***0.7 ± 0.1***	***98.2 ± 5.0***				***100.2 ± 5.0***
n-C_4H_{10}:N_2 (0.51:0.49)	49.8		0.3	0.1	0.1	0.3	49.4	0.0	9.7E−06	7.2E−03	
					600 °C						
n-C_4H_{10}			3.1	1.7	1.6	3.1	90.3	0.1	8.1E−04	0.1	
			2.4 ± 0.4	***1.6 ± 0.2***	***1.1 ± 0.1***	***2.7 ± 0.3***	***93.6 ± 4.7***				***101.4 ± 4.7***
n-C_4H_{10}:H_2O (0.5:0.5)		49.1	1.2	0.7	0.6	1.2	47.2	0.1	2.0E−04	3.1E−02	
			(2.3)	(1.4)	(1.2)	(2.3)	(92.6)				
			1.7 ± 0.3	***1.2 ± 0.2***	***0.7 ± 0.1***	***2.0 ± 0.2***	***93.7 ± 4.7***				***99.3 ± 4.7***
n-C_4H_{10}:N_2 (0.51:0.49)	49.1		1.2	0.7	0.6	1.2	47.2	0.1	1.9E−04	3.7E−02	
	47.1 ± 3.0		***1.8 ± 0.3***	***1.0 ± 0.1***	***0.4 ± 0.1***	***1.4 ± 0.2***	***48.2 ± 3.0***				***99.9 ± 4.3***
					650 °C						
n-C_4H_{10}			8.3	5.0	4.5	8.2	73.3	0.5	8.9E−03	0.3	
			7.1 ± 1.0	***4.6 ± 0.8***	***2.2 ± 0.2***	***6.5 ± 0.5***	***75.1 ± 4.0***				***95.5 ± 4.2***
n-C_4H_{10}:H_2O (0.5:0.5)		46.9	3.7	2.4	1.8	3.6	41.1	0.4	2.9E−03	0.1	
			(6.9)	(4.5)	(3.5)	(6.8)	(77.4)				
			5.5 ± 0.8	***4.1 ± 0.8***	***1.4 ± 0.1***	***5.5 ± 0.5***	***80.3 ± 4.0***				***96.8 ± 4.2***
n-C_4H_{10}:N_2 (0.51:0.49)	47.0		3.7	2.3	1.9	3.6	41.1	0.3	2.7E−03	0.1	
	44.4 ± 3.0		***3.9 ± 0.6***	***3.8 ± 0.7***	***1.3 ± 0.1***	***4.5 ± 0.5***	***41.5 ± 3.0***				***99.4 ± 4.4***
					700 °C						
n-C_4H_{10}			16.9	11.5	9.3	16.1	43.8	1.6	8.2E−02	0.9	
			22.4 ± 1.5	***15.7 ± 1.0***	***5.0 ± 0.5***	***16.4 ± 0.7***	***45.5 ± 3.0***				***105.0 ± 3.6***
n-C_4H_{10}:H_2O (0.5:0.5)		42.0	9.1	6.9	4.3	8.5	27.2	1.5	3.9E−02	0.5	
			(15.7)	(12.0)	(7.4)	(14.7)	(46.8)				
			25.8 ± 1.5	***20.3 ± 1.5***	***5.0 ± 0.5***	***18.3 ± 0.7***	***35.0 ± 3.0***				***104.4 ± 3.8***
n-C_4H_{10}:N_2 (0.51:0.49)	42.1		9.1	6.6	4.7	8.6	27.2	1.1	3.7E−02	0.5	
	41.1 ± 3.0		***14.7 ± 1.0***	***10.2 ± 0.8***	***2.5 ± 0.3***	***9.7 ± 0.6***	***27.1 ± 3.0***				***105.3 ± 4.5***
					750 °C						
n-C_4H_{10}			24.9	19.7	12.1	20.7	16.2	4.2	0.5	1.9	
n-C_4H_{10}:H_2O (0.5:0.5)		35.5	15.8	14.2	6.0	12.4	10.7	4.0	0.3	1.2	
			(24.5)	(22.0)	(9.2)	(19.2)	(16.5)				
n-C_4H_{10}:N_2 (0.51:0.49)	35.8		15.8	13.4	6.8	12.7	10.7	3.3	0.3	1.2	
					800 °C						
n-C_4H_{10}			29.5	26.2	10.5	18.1	4.2	7.3	1.5	2.6	
			36.3 ± 2.6	***39.8 ± 2.5***	***5.6 ± 0.5***	***13.0 ± 0.7***	***4.3 ± 0.4***				***99.0 ± 3.7***
n-C_4H_{10}:H_2O (0.5:0.5)		31.4	20.3	20.1	5.1	10.9	2.5	6.6	1.2	1.9	
			(29.7)	(29.3)	(7.4)	(15.9)	(3.7)				
			36.6 ± 2.6	***42.3 ± 2.5***	***3.8 ± 0.4***	***11.2 ± 0.7***	***4.1 ± 0.4***				***98.0 ± 3.7***
n-C_4H_{10}:N_2 (0.51:0.49)	31.7		20.4	19.2	6.0	11.2	2.5	6.0	1.2	1.9	
	31.3 ± 3.0		***28.5 ± 2.0***	***28.8 ± 2.0***	***3.2 ± 0.3***	***8.4 ± 0.6***	***2.9 ± 0.3***				***103.1 ± 4.2***

[a] C_5^+ denotes the sum of species having five or more carbons. [b] C_4^- denotes the sum of species with four or less carbons that are not CH_4, C_2H_4, C_2H_6, C_3H_6, and n-C_4H_{10}. [c] Cf. text for model input parameters. Observed species mole fractions are shown in bold italics. Normalized results for predicted mole fractions for fuel−steam mixtures are shown in parentheses. Normalization is accomplished via $x_{i,\text{normalize}} = x_i/(100 - x_{H_2O}) \times 100\%$.

600 °C. Experiments for all three different fuel inlet conditions were performed at 600 °C. The observed conversion is noticeably higher, ranging from 4 to 6%. For all the mixtures, the product selectivities are quite similar, with methane and propylene as the dominant products. Here the ethylene yield is noticeably higher than that for ethane.

650 °C. At 650 °C, the decrease in *n*-butane concentration begins to become more significant. (With a greater loss of reactant, combined with the fact that the number of moles increases as a result of reaction, the lower mole fraction observed for butane results both from actual loss of butane as well as simple dilution. A good illustration of this is the observed drop in the mole fraction of N_2 at higher temperatures.) For all mixtures, methane and propylene are still the dominant products, although the ethylene yield is comparable for the diluted nitrogen case. The ethylene yield is now substantially higher than that of ethane.

700 °C. There is a substantial increase in conversion and a noticeable tilt toward methane as the dominant product. The trend toward increasing ethylene yield continues; in both diluted cases it is now slightly larger than the propylene yield. The relative amount of ethane formed continues to decrease.

800 °C. At this temperature, virtually all the butane has been reacted. The trend in reaction yields continues, with ethylene now the dominant product for all the mixtures. Methane is the species with the next highest yield and is now much higher than propylene. Ethane remains the species with the lowest yield.

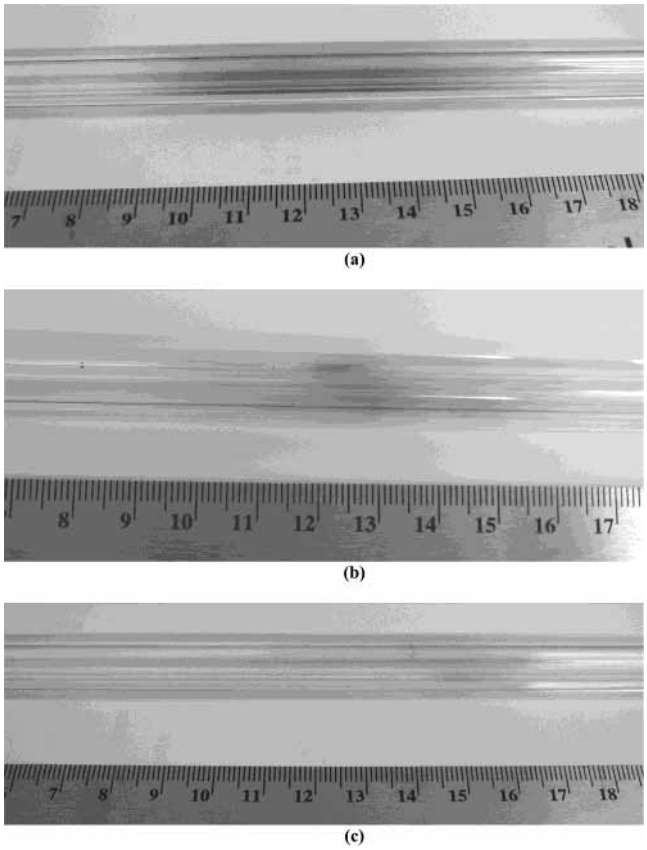

Figure 3. 6 mm i.d. quartz reactor after 4 h of operation at 700 °C with a nominal 5 s residence time: (a) 100% *n*-C_4H_{10}; (b) 50% *n*-C_4H_{10}: 50% N_2; (c) 50% *n*-C_4H_{10}:50% H_2O.

Deposit Formation. One of the major concerns with the use of hydrocarbon fuels in SOFCs is the propensity for deposit formation. In our experiments, qualitative observations of deposit formation were made by examining the quartz reactor after running a specific mixture through the reactor for 4 h. This approach indicated that there was no apparent deposit formation within the reactor for any of the mixtures at 650 °C and lower temperatures. As the reactor temperature was increased to 700 °C, with all other experimental conditions the same as at 650 °C, an obvious deposit on the inner walls of the quartz reactor was observed with the neat butane mixture, cf. Figure 3a. Less deposit was observed with the nC_4/N_2 mixture, cf. Figure 3b. Interestingly, deposit formation was negligible with the nC_4/H_2O mixture, cf. Figure 3c. The first inference from these qualitative observations is that dilution does play a role in minimizing deposit formation, as seen in comparing Figure 3a and 3b. This is to be expected, since the lower concentration of reactive species would be expected to decrease the rate of molecular weight growth leading to deposits. However, a qualitative comparison of the two diluted fuel cases, i.e. the nC_4/H_2O and the nC_4/N_2, indicates a significant difference in the amount of deposit formed. This suggests that the steam is either actively participating in inhibition of molecular weight growth or that it is participating in some type of gasification of the deposit. All three mixtures show significant deposit formation on the inner reactor walls at 800 °C.

Comparison To Model Predictions

Butane Conversion. The ratio of the predicted conversion of butane is compared to that observed for the neat and nC_4/N_2 mixture cases in Figure 4a. The modeling predictions are in excellent agreement with the observations for both the neat and the nC_4/N_2 mixtures. The predictions clearly capture the observed temperature dependence for both the neat and diluted mixture cases. From both the model predictions and the observed experimental data, it is also clear that the conversion for the neat *n*-butane case is higher than the nC_4/N_2 case. This difference is simply due to dilution of the butane for the nC_4/N_2 mixture. This good agreement, achieved without any modifications to the gas-phase kinetic mechanism, was very encouraging and suggests that the model can account for conversion of light hydrocarbons fuels under SOFC conditions.

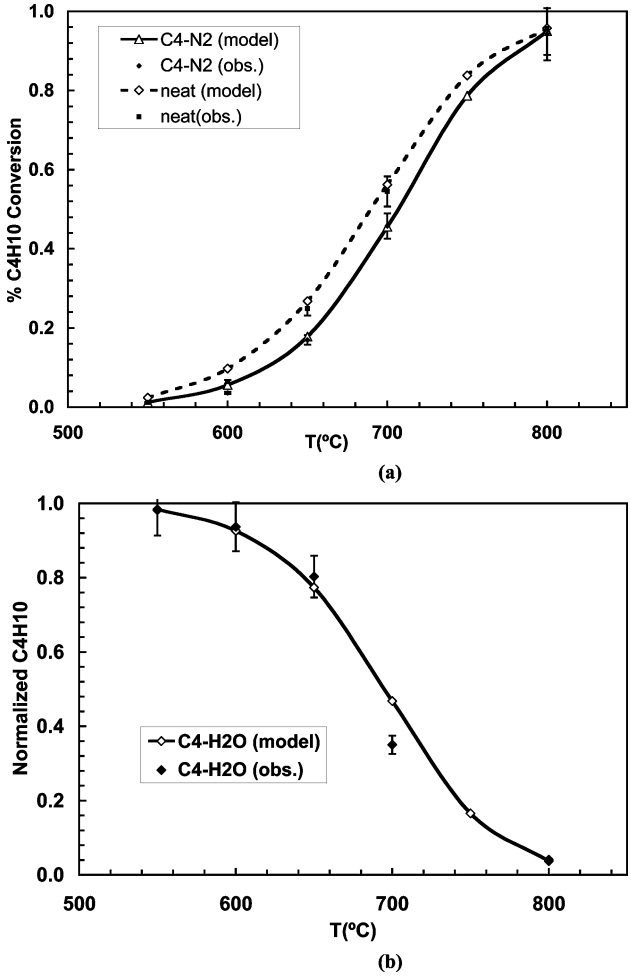

Figure 4. Comparison of modeling results to experimental data: (a) neat *n*-butane and 50% *n*-C_4H_{10}/50% N_2; (b) 50% *n*-C_4H_{10}/50% H_2O. Cf. text for normalization procedure used in part b.

The comparisons of the ratio of the final to initial *n*-butane mole fractions for the butane-steam mixture are shown in Figure 4b. As described earlier, the measured mole fractions exclude the water that was condensed prior to introduction to the GC. Thus, the modeling results were "normalized" by removing H_2O from the product profiles to allow for a direct comparison to that measured. With the notable exception of the comparison at 700 °C, the fit is very good; again capturing the strong observed temperature dependence. The 700 °C case is quite interesting; this was also the one case where no deposits were observed. These observations might be connected—perhaps both are due to heterogeneous reactions in the presence of steam, perhaps on the quartz surface or the presence of contaminants (especially trace levels of metals) on the quartz surface. The modeling results for the nC_4/N_2 mixture and the nC_4/H_2O mixture results were identical. This indicates that steam is not

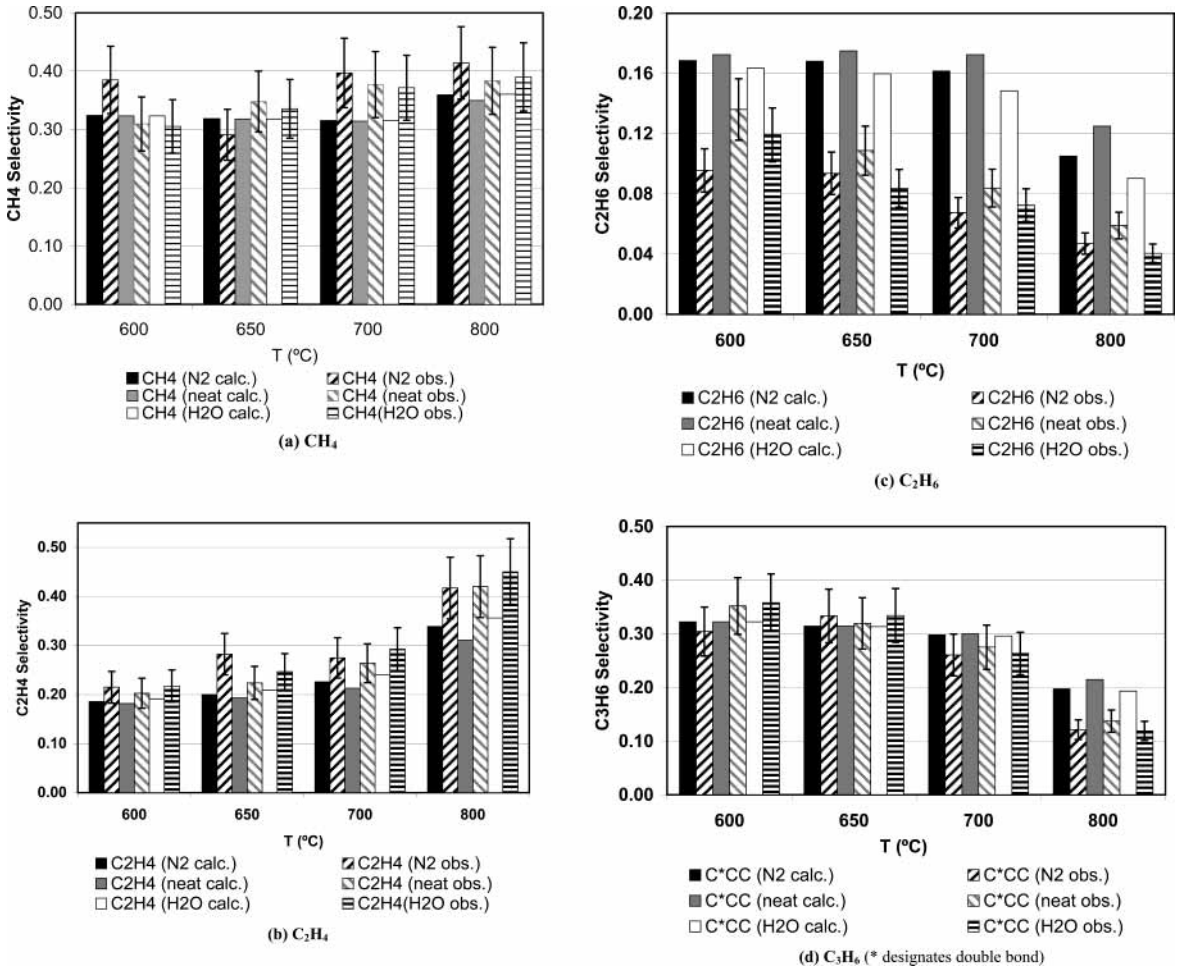

Figure 5. Comparisons between model predictions and experimental data for the selectivity for the major products from *n*-butane pyrolysis study. Selectivity (%) $= x_i/(x_{CH_4} + x_{C_2H_4} + x_{C_2H_6} + x_{C_3H_6}) \times 100\%$.

participating to any significant extent in the gas-phase kinetics, even though the gas-phase reactions such as

$$H_2O + n\text{-}C_4H_9 \Leftrightarrow n\text{-}C_4H_{10} + OH$$

are included in the mechanism. (In the mechanism, this reactions and others like it are written in the reverse direction).

Product Selectivity. The predicted product distributions are included in Table 1, and these are compared to the experimental observations in Figure 5. For ease of comparison, the distributions are shown in terms of product selectivity. Figure 5a compares the predicted and observed temperature dependence of the selectivity to methane. Overall the agreement is encouraging, with the predictions capturing the slight increase with temperature and showing little effect of mixture composition. The ethylene selectivity comparisons are shown in Figure 5b**.** Although the model predicts selectivities slightly lower than observed, it clearly captures the sharp upswing between 700 and 800 °C. Both model and data show little difference in selectivity among the three mixtures. The ethane selectivity, shown in Figure 5c does not show a good match between the model and experiment. The predicted ethane selectivity is too high and, although it does predict the observed decline with temperature, the predicted decline becomes large only above 700 °C, while the data demonstrate a more gradual decline throughout the temperature range. It is interesting to note that the small shift in selectivity with mixture composition, with the highest selectivity for the neat butane case, is predicted by the model. The propylene selectivity comparisons are shown in Figure 5d. The model predictions are in generally good agreement with the experimental data, with the exception that only a portion of the sharp decline at 800 °C is predicted. Any difference for the different mixtures is well within the experimental error.

Deposit Formation. Since the model contains a reasonably complete description of gas-phase molecular weight growth, we used these results to attempt to connect to the observed deposit formation. In particular, we considered all species above C_4 (which will be denoted as C_5^+) as potential deposit precursors. These results are included in Table 1. The predicted C_5^+ values for the steam and nitrogen dilution cases are very similar. This is consistent with our observation that any gas-phase reactions of steam are very slow under these conditions, and thus steam is simply acting as a diluent, just like nitrogen. This is in contrast to the experimental observations that steam diminished deposit formation. Our modeling results suggest that this cannot be explained by gas-phase reactions, and is probably due to heterogeneous reactions. Note that the ratio of C_5^+ predicted for the neat butane case to that of the diluted mixtures decreases from approximately five at 550 °C to only slightly greater than unity at 800 °C. Thus, at the higher temperatures, the predictions suggest that the inhibition of deposit formation by dilution is much less effective than at lower temperatures.

Figure 6 shows the predicted effect of temperature on formation of C_5^+ for the various mixtures. The dramatic increase in deposit precursors near 700 °C is consistent with the observed

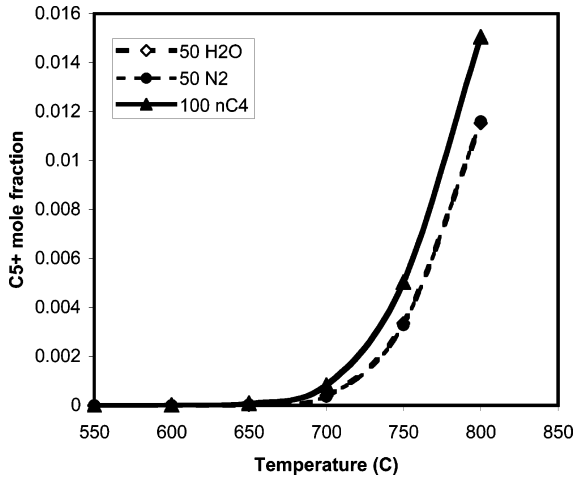

Figure 6. Modeling results showing increase in mole fraction of C_5^+ species with temperature.

onset of deposits at this temperature, as shown in Figure 3. Also consistent with the experimental observations, the predictions indicate a lower temperature threshold for the neat butane case.

The major C_5^+ species formed in all mixtures at 700 °C is cyclopentene, with 1,3-cyclopentadiene having the next highest mole fraction. Both are indeed likely deposit precursors, in that they are stable unsaturated ring compounds, susceptible to radical addition reactions leading to even more molecular weight growth. Furthermore, 1,3-cyclopentadiene has an unusually weak C−H bond, allowing relatively facile formation of the resonantly stabilized cyclopentadienyl radical. There are several routes leading from this species to higher molecular weight molecules.

Other Products. Table 1 also includes the predicted mole fractions of H_2 and the sum of minor C_4^- species, i.e., other than those specifically listed in the table. Note that production of H_2 increases substantially with increasing temperature. At 800 °C, this mole fraction is ∼7%, suggesting that the sum of mole fractions of the measured hydrocarbons (Table 1) might be slightly too large at 800 °C. As discussed earlier, the measured sum at 700 °C is likely slightly high. The computed mole fractions of C_4^- species are generally consistent with the experimental observations that such species are only observed in trace amounts.

Sensitivity Analysis

As seen above, the predictions from the unadjusted kinetic model are in reasonable agreement with the observed data. However, this is obviously a very large mechanism and a sensitivity analysis was performed to determine whether some smaller subset of the reactions were responsible for much of the observed kinetics. The sensitivity analyses were performed using the SENKIN driver program from the CHEMKIN Collection v. 3.6.2 suite programs using the experimental temperature profile at 700 °C.[29]

The results from the sensitivity analysis are shown in Figure 7, parts a−e, for the five species of interest, i.e. CH_4, C_2H_4, C_2H_6, C_3H_6, and *n*-C_4H_{10}. It is interesting to note that, although the system consists of ∼2500 reactions, there are only 11 reactions whose rates significantly affect the formation or consumption of the five species of interest. These reactions are listed in Table 2.

Figure 7a shows the normalized sensitivity coefficients for methane. The reaction with the largest positive coefficient is R1. A positive sensitivity coefficient means that an increase in the rate coefficient will lead to an increase in the species of interest. Since CH_4 is a product of R1, this is not surprising. Another reason for the importance of this reaction is that the other product, the secondary butyl radical, will undergo a rapid β-scission to form CH_3 + propylene, and this methyl radical will form methane via hydrogen abstraction. The second most positive coefficient is ethyl abstracting the secondary hydrogen in butane (R3), which also forms a secondary butyl radical. Lower positive sensitivities are calculated for the dissociation reactions R5 and R6. In terms of inhibiting formation of methane, note that all of these reactions (R7, R8, and R10) form the allyl radical. Allyl is resonantly stabilized, and thus is quite unreactive. Note that R7 inhibits methane formation even though it forms a methyl radical. R8 and R10 have the effect of replacing an active radical, either CH_3 or C_2H_5, with allyl. Even though the total number of radicals remains the same, the net activity drops substantially.

The results for ethylene are shown in Figure 7b. These illustrate the very important role that abstraction from butane plays in determining the product distribution. The most sensitive reactions for ethylene production are the abstractions from butane by CH_3 and C_2H_5. The two most positive contributions to the formation of ethylene are R2 and R4, which produce *n*-C_4H_9, while the most negative contributions are R1 and R3, which produce *s*-C_4H_9. R2 and R4 favor ethylene production since the *n*-C_4H_9 will undergo rapid β-scission to form C_2H_5 + C_2H_4, a direct channel for ethylene formation. R1 and R3 inhibit ethylene formation since the secondary butyl radical formed by these abstractions is the primary pathway to the complementary products methane and propylene. Thus, one might view methane and propylene production as a marker for production of the secondary butyl radical and ethane and ethylene production as the corresponding marker for production of the *n*-butyl radical. The sensitivities of the dissociation reactions R5 and R6 are comparable to that seen for methane.

The ethane sensitivity is shown in Figure 7c. The four most important reactions are precisely those reported for ethylene, confirming the importance of the rapid β-scission reactions for the butyl radicals. The main difference here is that the ethyl radical formed by β-scission of *n*-C_4H_9 must first abstract an H atom from a stable hydrocarbon to form ethane. For this case, the dissociation reaction producing ethyl radicals (R6) is more important than R5, which does not produce C_2 species. The new reaction identified in the sensitivity analysis is the β-scission of C_2H_5 to form ethylene (R9 running in reverse). This pathway competes with the ethyl abstraction pathway, diminishing the ethane yield and increasing that of ethylene. Increasing this rate coefficient is one way to try to improve the overprediction of ethane (and underprediction of ethylene) in the model.

The sensitivity analysis of propylene is shown in Figure 7d. It is not surprising at this stage to see that the two reactions with the highest positive sensitivity are R1 and R3, similar to methane (cf. Figure 7a). The secondary butyl radical will undergo β-scission to form propylene plus methyl. As seen above, the next set of reactions are the two dissociation reactions R5 and R6. We again see the inhibiting effect of formation of allyl radicals (R7 and R8). Formation of the primary butyl radical **(**R2**)** also inhibits propylene production, but interestingly it becomes important at later times than allyl formation.

Figure 7e shows the sensitivity analysis for *n*-butane. Here the sensitivity coefficients are smaller than for product formation. Since we are looking at consumption of butane, rather than formation of products, a positive sensitivity coefficient for this case means that an increase in the rate coefficient leads to a

TABLE 2: Rate Constant Parameters for the Most Sensitive Reactions for Formation and Consumption of Major Species in *n*-Butane Pyrolysis, Where $k = AT^n \exp(-E_a/RT)$, with Units of mol cm^3 s

	reaction	*A*	*n*	E_a (cal/mol)	*k* (1000 K)
R1	$C_4H_{10} + CH_3 \leftrightarrow CH_3CH_2C^{\bullet}HCH_3 + CH_4$	3.26E+06	1.87	8908	1.47E10
R2	$C_4H_{10} + CH_3 \leftrightarrow CH_3CH_2CH_2CH_2^{\bullet} + CH_4$	4.89E+06	1.87	10 630	9.27E9
R3	$C_4H_{10} + C_2H_5 \leftrightarrow CH_3CH_2C^{\bullet}HCH_3 + C_2H_6$	2.64E+04	2.51	9910	6.11E9
R4	$C_4H_{10} + C_2H_5 \leftrightarrow CH_3CH_2CH_2CH_2^{\bullet} + C_2H_6$	3.96E+04	2.51	11 632	3.85E9
R5	$C_4H_{10} \leftrightarrow CH_3CH_2C^{\bullet}H_2 + CH_3$	6.51E+20	−1.291	87 067	8.14E−3
R6	$C_4H_{10} \leftrightarrow C_2H_5 + C_2H_5$	1.04E+22	−1.737	86 472	8.05E−3
R7	$CH_2{=}CH_2CH_2CH_3 \leftrightarrow CH_2{=}CH_2C^{\bullet}H_2 + CH_3$	1.66E+80	−18.78	110 973	4.22E−1
R8	$C_3H_6 + CH_3 \leftrightarrow CH_2{=}CH_2C^{\bullet}H_2 + CH_4$	7.89E+05	1.87	8032	5.64E9
R9[a]	$C_2H_4 + H \leftrightarrow C_2H_5$				1.30E12
R10	$C_3H_6 + C_2H_5 \leftrightarrow CH_2{=}CH_2C^{\bullet}H_2 + C_2H_6$	6.34E+03	2.51	9034	2.28E9
R11	$CH_2{=}CH_2C^{\bullet}H_2 + C_2H_4 \leftrightarrow$ cyclopentene + H	4.44E+11	−0.42	12 438	4.66E7

[a] Computed using Troe falloff parameters; value shown is for 0.8 atm.

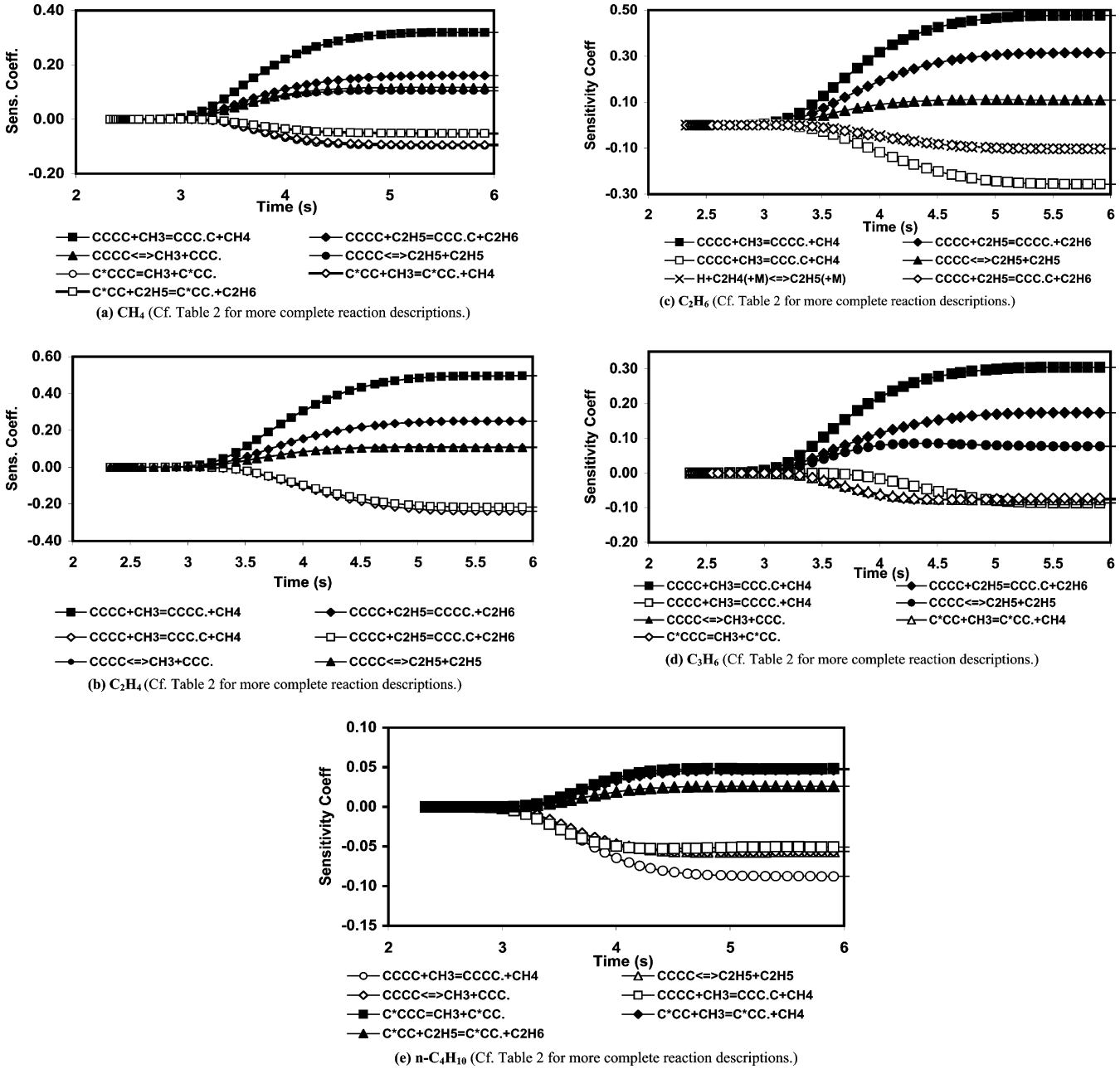

(a) CH_4 (Cf. Table 2 for more complete reaction descriptions.)

(c) C_2H_6 (Cf. Table 2 for more complete reaction descriptions.)

(b) C_2H_4 (Cf. Table 2 for more complete reaction descriptions.)

(d) C_3H_6 (Cf. Table 2 for more complete reaction descriptions.)

(e) n-C_4H_{10} (Cf. Table 2 for more complete reaction descriptions.)

Figure 7. Sensitivity Analysis for the five major species of interest in *n*-butane pyrolysis determined by SENKIN analysis at 700 °C: (a) CH_4; (b) C_2H_4; (c) C_2H_6; (d) C_3H_6; (e) *n*-C_4H_{10}.

higher concentration of butane at a given time, i.e., the reaction inhibits conversion. Thus, it is not surprising to see all of the positive sensitivities involve reactions (R7, R8, and R10) that form allyl radicals. Butane consumption is promoted by both the abstraction reactions R1 and R2 as well as the dissociation reactions R5 and R6.

The kinetic model predicted that cyclopentene is the major deposit precursor. A rate analysis for this species revealed that

one chemically activated reaction

$$CH_2{=}CHC^{\bullet}H_2 + C_2H_4 \Leftrightarrow \text{cyclopentene} + H \quad \text{(R11)}$$

is responsible for most of the cyclopentene formed. This reaction represents a combination of events. Initially a linear unsaturated radical is formed by addition. This energized radical has sufficient energy to form the cyclopentyl radical by radical addition to the double bond. This species (still energized) then ejects a hydrogen atom via β-scission to form cyclopentene. The sensitivity analysis showed that cyclopentene production is most influenced by this rate coefficient. The other reactions that influence formation of this deposit precursor are R2, R5, and R6. R3 and R7 inhibit cyclopentene production. Thus, even formation of the deposit precursors are dominated by the same small subset of reactions. R2 produces n-C_4H_9, the primary precursor of the reactant ethylene, while the butane dissociation reactions R5 and R6 increase the radical pool. The fact that R7 is the main inhibiting reaction, even though it produces the reactant allyl radical, indicates the importance of maintaining an active radical pool for molecular weight growth; as discussed above, formation of allyl, relative to more active radicals like H, CH_3 and C_2H_5 inhibits the overall reactivity of the system, including molecular weight growth. R3 inhibits growth since this reaction consumes C_2H_5, thus lowering the formation rate of ethylene and H atoms via β-scission of ethyl.

Rate Coefficient Comparison To Literature Values

Given that both butane conversion as well as formation of the major and minor products are primarily governed by the rates of only 11 reactions, the next step is to compare our values for these rate coefficients with those available in the literature. Earlier we made the point that it was possible to obtain a reasonable agreement between our model and the data without making any adjustments to the model. It is equally important to demonstrate that the rate coefficients that we used for these reactions are reasonable. In Table 2, we list the rate coefficients in our kinetic model for the 11 reactions discussed above. We will compare these expressions, evaluated at 1000 K, to those that are available from the literature, e.g., to values that are compiled in the NIST kinetics database.[30]

For R1, there are no direct measurements listed at any temperature in the NIST kinetics database. An earlier compilation[31] reports several values measured at lower temperatures. The average measured value at 500 K is 2.6×10^7 cm^3 mol^{-1} s^{-1}. The coefficient used in this work is 4.6×10^7 cm^3 mol^{-1} s^{-1} at 500 K, in reasonable agreement with the measurements. A similar situation exists for R2; there are no measurements reported in the NIST database. The CRC tabulation reports 4.6×10^6 cm^3 mol^{-1} s^{-1} at 500 K, while the value in our model is 1.2×10^7 cm^3 mol^{-1} s^{-1} at 500 K.

R3 and R4 involve abstraction by ethyl radicals. NIST reports a value for the total abstraction rate coefficient from butane in our temperature range, which is 5×10^9 cm^3 mol^{-1} s^{-1} at 1000 K. Our combined value, including abstraction for both n-C_4H_9 and s-C_4H_9, is 1×10^{10} cm^3 mol^{-1} s^{-1}. We consider this to be reasonable agreement.

Comparisons of the dissociation rate coefficients (R5, R6, and R7) must take into account pressure-dependent falloff effects. For R5, our value is just beginning to enter the falloff regime, with $k/k_\infty = 0.72$ at 1000 K. The value we used for k_∞ for R5 is approximately three times lower than the estimates in the NIST database, but it is in good agreement with the recently measured value of R(-6). The k_∞ value for R6 is based on the recent direct measurement of the reverse reaction by Shafir et al.,[23] and that value is only slightly lower than that listed in NIST for this reaction. As with R5, our rate coefficient is $\sim 0.7k_\infty$, reflecting falloff effects. There is a substantial spread in reported values for the unimolecular dissociation of 1-butene, R7.[30,32−34] The value that we used is close to the average of those listed; at 1000 K, it is close to the high-pressure limit. The much higher rate coefficient for R7, relative to R5 and R6, is due to the substantially weaker C−C bond in 1-butene due to formation of the resonantly stabilized allyl radical.

The β-scission of the ethyl radical is described in our mechanism in terms of the reverse reaction R9. Our value (and the pressure dependence) was taken directly from the GRI 2.11 mechanism.[35] This reaction is well into the falloff region. The GRI value of k_∞ is $\sim$70% of the value suggested by Baulch et al.[36]

R8 and R10 are abstractions from propylene. Both of these rate coefficients are in good agreement with the recommendations of Tsang that are included in the NIST database.[30,37] There are again no direct measurements of R11. This rate coefficient estimate was based on a chemical activation analysis and is approximately 2.5 times larger than that reported in NIST. The NIST value is based on fitting to a complex mechanism.

In summary, the most sensitive reactions in our unadjusted mechanism have rate coefficients that are reasonably consistent with literature values. We are encouraged by this comparison, but clearly recognize that the overall good agreement between our predictions and the butane pyrolysis data cannot be taken as evidence that each of our rate coefficient assignments is correct. Such an assertion requires explicit measurements of much less complex systems. The comparison to the available literature data suggests that our abstraction reaction rate coefficients are generally slightly higher. As discussed earlier, our abstraction rate coefficients are based on an extensive analysis of systems where reliable data are available. We have systematically extended these values to analogous systems, e.g., abstraction by ethyl, using standard thermochemical kinetics principles. In particular, we have taken care to properly account for the constraints imposed by microscopic reversibility to ensure that forward and reverse estimates are thermodynamically consistent. We have also explicitly accounted for the non-Arrhenius behavior expected for abstraction reactions in the temperature range of this study.

Kinetics Overview

It appears that butane pyrolysis can be accurately described in terms of a straightforward Rice−Herzfeld mechanism. After initiation by breaking the C−C bonds in butane, the radicals formed abstract from the parent to form n-C_4H_9 and s-C_4H_9 radicals. These radicals can then react as follows:

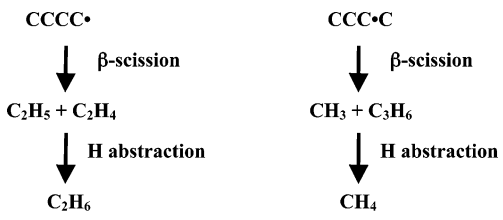

The primary radicals lead to the C_2 products while the secondary radicals lead to the C_1 and C_3 products. The increase in C_2 products with increasing temperature, and the corresponding decrease in production of methane and propylene, is due to the higher activation energies of the abstraction reactions that form

the *n*-butyl radical. Thus, the selectivity to these two product pairs can be traced to the selectivity of forming the two butyl radicals. An interesting complication is that the propylene product has an easily abstractable hydrogen, and the formation of allyl acts to inhibit conversion by modifying the nature of the free radical pool. This same allyl radical was also shown to be responsible for the small amounts of molecular weight growth observed since it can add to ethylene, forming cyclopentene and H. This pathway is accelerated since it is chemically activated, and the initially energized linear adduct can directly form the cyclic species prior to collisional stabilization. An essential component of this scheme is β-scission of the butyl radicals, although these reactions do not exhibit high rate coefficient sensitivities. The reason for this is that these β-scission reactions are so fast at these temperatures that they are not rate-limiting.

Implication of Results To SOFC Studies

These results show that it is important to take into account the homogeneous reactions of hydrocarbon fuels in high temperature fuel cells. In general, these kinetics can have major impact into two distinct areas: (1) The species that will undergo electrochemical reaction might be far removed from the parent fuel delivered to the fuel cell. In practice, even bigger changes in the nature of the species undergoing electrochemical reaction will be expected since there will likely be catalytic reactions with the metal in the porous anode as the species are being transported to the three-phase boundary region. (2) These gas-phase reactions have been shown to lead to molecular weight growth, perhaps leading to deposit formation. An additional experimental observation is that it appears that even a quartz/steam system is enough to inhibit deposit formation. One might expect this effect to be even more evident in a real fuel cell with the anode metal acting as a catalyst for this reaction.

Summary

To explore this possibility of gas-phase chemistry in the anode channel of a SOFC, experiments using *n*-butane as a representative hydrocarbon fuel were conducted under SOFC conditions. Butane conversion and product formation were monitored in quartz reactor experiments at $P \sim 0.8$ atm, $\tau \sim 5$ s, and $T = 550-800$ °C. Three different fuel mixtures were used: neat *n*-butane, 50% *n*-C_4H_{10}/50% H_2O and 50% *n*-C_4H_{10}/50% N_2. These experiments demonstrate that substantial gas-phase chemistry does occur, and that this must be accounted for when predicting fuel cell efficiency. These data were compared to predictions using a plug-flow model that incorporated the experimentally measured temperature profile along the reactor. Comparisons of the model predictions to the experimental data show that the model, without any modifications, captures the observed strong temperature dependence of *n*-butane conversion and is also able to capture the changes in product selectivity with temperature for the neat butane and the diluted butane mixtures. The model also properly predicts the observed onset of deposit formation near 700 °C. Both conversion and selectivity are shown to be sensitive to only a very small subset of the reactions in the mechanism. Comparison of the rate coefficients of this subset to literature values, where available, are generally reasonable and suggest that the kinetic model employed is adequate for describing reactions of small hydrocarbons in the anode channels of a SOFC. Thus, such models should provide a useful tool to estimate the importance of gas-phase chemistry for various proposed SOFC operating conditions.

Acknowledgment. The authors would like to thank ITN Energy Systems, Inc. for the use of their facilities, where the experimental work was conducted under DARPA Contract MDA972-01-C-0068. The authors appreciate Katie O'Gara's contributions to the experiment and data compilation. We also would like to thank Hans-Heinrich Carstensen and Chitral Naik for providing some of the elementary reaction rates used in the current model. Chitral Naik also performed some of the modeling calculations.

Supporting Information Available: The mechanism and thermodynamic database, in CHEMKIN format, and tables of the temperature profiles used for the modeling. This material is available free of charge via the Internet at http://pubs.acs.org.

References and Notes

(1) Brouwer, J. Solid-oxide Fuel Cell − Emergence of a Technology. *Fuel Cell Catalyst* **2000**, *1*, 1.
(2) Zhu, H.; Kee, R. J. *J. Power Sources* **2003**, *117*, 61−74.
(3) Wang, X.; Gorte, R. J. *Catal. Lett.* **2001**, *73*, 15−19.
(4) Borowiecki, T. *Appl. Catal.* **1982**, *4*, 233.
(5) Borowiecki, T.; Golebiowski, A. *Catal. Lett.* **1994**, *25*, 309.
(6) Borowiecki, T.; Golebiowski, A.; Stasinska, B. *Appl. Catal. A* **1997**, *153*, 141.
(7) Kepinski, L.; Stasinska, B.; Borowiecki, T. *Carbon* **2000**, *38*, 1845−1856.
(8) Trimm, D. L. *Catal. Today* **1997**, *37*, 233.
(9) Tracz, E.; Scholz, R.; Borowiecki, T. *Appl. Catal.* **1990**, *66*, 133.
(10) Trimm, D. L. *Catal. Today* **1999**, *49*, 3.
(11) Hickman, D. A.; Haupfear, E. A.; Schmidt, L. D. *Catal. Lett.* **1993**, *17*, 223.
(12) Hickman, D. A.; Schmidt, L. D. *Science* **1993**, *259*, 343.
(13) Hickman, D. A.; Schmidt, L. D. *AIChE J.* **1993**, *39*, 1164.
(14) Otsua, K.; Wang, Y.; Sunada, E.; Yamanaka, I. *J. Catal.* **1998**, *175*, 152.
(15) Tsang, S. C.; Claridge, J. B.; Green, M. L. H. *Catal. Today* **1995**, *23*, 3.
(16) Krummenacher, J. J.; West, K. N.; Schmidt, L. D. *J. Catal.* **2003**, *215*, 332−343.
(17) Walters, K. M.; Dean, A. M.; Zhu, H.; Kee, R. J. *J. Power Sources* **2003**, *123*, 182−189.
(18) Hepp, H. J.; Frey, F. E. *Ind. Eng. Chem* **1953**, *45*, 410.
(19) Weisel, M. D.; Chang, A. Y.; Zhong, X.; Dean, A. M. The Pyrolysis and Oxidation of N−Butane & Isobutane: A Flow Tube Reactor Molecular Beam Mass Spectrometry Study. Presented at the Fourth International Conference on Chemical Kinetics, 1997, Gaithersburg, MD.
(20) Mallinson, R. G.; Braun, R. L.; Westbrook, C. K.; Burnham, A. K. *Ind. Eng. Chem. Res.* **1992**, *31*, 37−44.
(21) *CRC Handbook of Chemistry and Physics*, 63rd. ed.; Weast, Robert, C., Ed.; CRC Press: Boca Raton, FL, 1982.
(22) Mims, C. A.; Mauti, R.; Dean, A. M.; Rose, K. D. *J. Phys. Chem.* **1994**, *98*, 13357−13372.
(23) Shafir, E. V.; Slagle, I. R.; Knyazev, V. D. *J. Phys. Chem. A* **2003**, *107*, 6804−6813.
(24) Dean, A. M.; Bozzelli, J. W. In *Gas-Phase Combustion Chemistry*; Gardiner, W. C., Ed.; Springer: Berlin, 2000; pp 125−341.
(25) Chang, A. Y.; Bozzelli, J. W.; Dean, A. M. *Z. Phys. Chem.* **2000**, 1533−1568.
(26) Benson, S. W. *Thermochemical Kinetics*, 2nd ed.; Wiley-Interscience: New York, 1976.
(27) Ritter, E.; Bozzelli, J. W. *Int. J. Chem. Kinet.* **1991**, *23*, 767−778.
(28) Lay, T. H.; Bozzelli, J. W.; Dean, A. M.; Ritter, E. R. *J. Phys. Chem.* **1995**, *99*, 14514−14527.
(29) Kee, R. J.; Rupley, F. M.; Miller, J. A.; Coltrin, M. E.; Grcar, J. F.; Meeks, E.; Moffat, H. K.; Lutz, A. E.; Dixon-Lewis, G.; Smooke, M. D.; Warnatz, J.; Evans, G. H.; Larson, R. S.; Mitchell, R. E.; Petzold, L. R.; Reynolds, W. C.; Caracotsios, M.; Stewart, W. E.; Glarborg, P.; Wang, C.; Adigun, O. CHEMKIN Collection. [Release 3.6.2]. 2000. San Diego, CA, Reaction Design.
(30) NIST Chemical Kinetics Database. Release 1.1, 2000. http://kinetics.nist.gov/.
(31) *CRC Handbook of Bimolecular and Termolecular Gas Reactions*; Kerr, J. A., Moss, S. J. Eds.; CRC Press: Boca Raton, FL, 1981, Vol. 1
(32) Dean, A. M. *J. Phys. Chem.* **1985**, *89*, 4600.
(33) Halstead, M. P.; Quinn, C. P. *Trans. Faraday Soc.* **1968**, *64*, 103.

(34) Trenwith, A. B. *Trans. Faraday Soc.* **1970**, *66*, 2805−2811.
(35) Bowman, C. T.; Hanson, R. K.; Davidson, D. F.; Gardiner, W. C., Jr.; Lissianski, V.; Smith, G. P.; Golden, D. M.; Frenklach, M.; Goldenber, M. GRI-Mech 2.11. 4−16−1996. http://www.me.berkeley.edu/gri_mech/.
(36) Baulch, D. L.; Cobos, C. J.; Cox, R. A.; Frank, P.;.Hayman, G.; Just, Th.; Kerr, J. A.; Murrells, T.; Pilling, M. J.; Troe, J.; Walker, R. W.; Warnatz, J. *J. Phys. Chem. Ref. Data* **1994**, *23*, 847−1033.
(37) Tsang, W. *J. Phys. Chem. Ref. Data* **1991**, *20*, 221−273.